

Instabilities, pattern formation, and mixing in active suspensions

David Saintillan¹ and Michael J. Shelley²

¹*Department of Mechanical Science and Engineering, University of Illinois at Urbana-Champaign, Urbana, Illinois 61801, USA*

²*Courant Institute of Mathematical Sciences, New York University, New York, New York 10012, USA*

(Received 7 July 2008; accepted 14 November 2008; published online 17 December 2008)

Suspensions of self-propelled particles, such as swimming micro-organisms, are known to undergo complex dynamics as a result of hydrodynamic interactions. To elucidate these dynamics, a kinetic theory is developed and applied to study the linear stability and the nonlinear pattern formation in these systems. The evolution of a suspension of self-propelled particles is modeled using a conservation equation for the particle configurations, coupled to a mean-field description of the flow arising from the stress exerted by the particles on the fluid. Based on this model, we first investigate the stability of both aligned and isotropic suspensions. In aligned suspensions, an instability is shown to always occur at finite wavelengths, a result that extends previous predictions by Simha and Ramaswamy [“Hydrodynamic fluctuations and instabilities in ordered suspensions of self-propelled particles,” *Phys. Rev. Lett.* **89**, 058101 (2002)]. In isotropic suspensions, we demonstrate the existence of an instability for the active particle stress, in which shear stresses are eigenmodes and grow exponentially at long scales. Nonlinear effects are also investigated using numerical simulations in two dimensions. These simulations confirm the results of the stability analysis, and the long-time nonlinear behavior is shown to be characterized by the formation of strong density fluctuations, which merge and breakup in time in a quasiperiodic fashion. These complex motions result in very efficient fluid mixing, which we quantify by means of a multiscale mixing norm.
© 2008 American Institute of Physics. [DOI: [10.1063/1.3041776](https://doi.org/10.1063/1.3041776)]

I. INTRODUCTION

The complex dynamics that arise in large-scale collections of self-propelled interacting particles have received much attention over the last several years. These systems, also known as *active suspensions*, are common in nature, where bacteria and other micro-organisms often develop in large-scale colonies,^{1,2} but also occur in technological applications, as engineers have tried to design artificial swimmers to perform various functions.^{3–7} As they propel themselves through the fluid, swimming particles induce disturbance flows, which cause them to interact hydrodynamically and result in complex collective motions in large suspensions. The chaotic nature of these motions has been observed in experiments, where it was found that they lead to enhanced hydrodynamic diffusion.^{8,9} In addition, in fairly concentrated suspensions, large-scale swirling motions and concentration patterns have also been reported.^{10–15} All of these effects were also confirmed in numerical simulations.^{16–18} While these patterns are common in situations where the particles are interacting with boundaries or external fields, as in bioconvection,^{1,2,19–21} they also occur in bulk suspensions,^{10–12,18,22} suggesting that interactions in these systems will cause a uniform suspension to evolve toward inhomogeneous configurations. In this paper, we show that these phenomena may be the result of fluid instabilities, and we identify mechanisms leading to this pattern formation.

Different types of swimmers may use a wide variety of swimming mechanisms, such as flagellar propulsion,^{5,6,23} beating cilia,²³ surface distortions,²⁴ chemical reactions,^{3,4,7} or actin-tail polymerization.^{25,26} In spite of the significant

differences between these various mechanisms, universal features exist in the associated hydrodynamics. In particular, a self-propelled particle exerts a propulsive force \mathbf{F}_p on the surrounding fluid, which must be balanced by the resistive drag due to the fluid, or $\mathbf{F}_d = -\mathbf{F}_p$. To leading order, the particle therefore exerts a force dipole on the fluid, the strength of which we denote by σ_0 in the subsequent discussion (cf. Sec. II). Depending on the mechanism for swimming, σ_0 can be either positive or negative: A particle that swims using its tail (*pusher*) will result in $\sigma_0 < 0$, whereas a particle that swims using its head (*puller*) will result in $\sigma_0 > 0$. As we will see, these two types of particles produce qualitatively different dynamics. In all cases, however, this dipole forcing induces a disturbance flow in the fluid, the characteristics of which are universal in the far field (i.e., far away from the particle surface) for a wide variety of particles. This observation has been the key to developing theoretical and numerical models for active particle suspensions^{16,27,28} and is the basis for the model described herein.

Hydrodynamic interactions among self-propelled particles have been studied in numerical simulations with various levels of approximation. Detailed boundary integral simulations have been proposed to accurately simulate interactions between nearby swimmers.²⁹ Such simulations, however, are very costly and typically limited to a few interacting particles. In order to capture the large-scale patterns that occur when many particles interact, simpler models have been developed based on the remark made above that the far-field disturbance of an individual swimmer is a dipole flow. Such a model was proposed by Hernández-Ortiz *et al.*,^{16,17} who

represented self-propelled particles as rigid dumbbells exerting a force dipole on the fluid. Based on this model, they were able to simulate fairly large suspensions of interacting swimmers in a parallel plate geometry and captured qualitative features of experiments on bacterial suspensions.⁸ In particular, they observed that, beyond a certain particle concentration, correlated motions started to appear and occurred on length scales much larger than the particle dimensions. They also reported an enhanced diffusion due to the motion of the particles. Recently, Ishikawa *et al.*^{30–33} also performed simulations of collections of swimming spheres based on a Stokesian dynamics algorithm and reported similar findings. Note that the majority of these previous simulations only considered the case of pushers ($\sigma_0 < 0$).

In our recent work,¹⁸ we proposed a detailed model based on slender-body theory³⁴ in which swimming particles are modeled as rigid slender rods that propel themselves by exerting an axisymmetric shear stress upon the surrounding fluid. This may represent the integrated effect of beating cilia on the surface of a micro-organism. Suspensions of up to 2500 particles with periodic boundary conditions and in thin films were simulated, and similar features as obtained by Hernández-Ortiz *et al.*¹⁶ were observed. In particular, large-scale correlated motions were found to develop regardless of the initial condition (aligned or random isotropic). We also found that the final microstructure at steady state in suspensions of pushers was not random but contained large density fluctuations, and that particles tended to align locally as a result of hydrodynamic interactions. In these simulations, no significant alignment was found in suspensions of pullers, where correlated motions were also found to be much weaker.

To overcome the size limitations of particle-based simulations, which are typically very costly, kinetic models have also become popular to describe suspensions over length scales much larger than the particle dimensions. In the context of self-propelled particles, such models have received much attention to describe the phenomenon of flocking in systems where interactions are purely local.^{35,36} Such models, however, cannot be applied to describe Stokes suspensions (such as bacterial suspensions), in which long-range hydrodynamic interactions are predominant and cannot be neglected. These models, however, can be generalized by coupling the evolution equations for the particle configurations to equations for the fluid flow. A noteworthy example was performed by Ramaswamy and co-workers:^{27,36–38} In their model, dynamical equations for liquid crystals were adapted to the case of rodlike self-propelled particles and coupled to the Navier–Stokes equations for the fluid flow, in which a coarse-grained active stress tensor representing the effect of the force dipole on individual particles was included. Using their model, they were able to investigate the stability of aligned suspensions and predicted that in the Stokes flow regime aligned suspensions should be unstable at long wavelengths for a specific range of wave angles with respect to the direction of alignment.²⁷

In the present work, we describe a simple kinetic model, previously introduced in Ref. 28, to study the dynamics in dilute suspensions of self-propelled particles embedded in a

Stokes fluid (Sec. II). The model is based on first principles, namely, a conservation equation for the particle configuration distribution, coupled to equations of motion for a self-propelled rod in a local linear flow and to the Stokes equations for the fluid motion, where an active stress representing the forcing due to the particles is included. Similar models have been used successfully in the past to describe the behavior of passive rod suspensions.^{39,40} Using this model in Sec. III, we analyze the linear stability of both aligned and isotropic suspensions: We show, in particular, that both types of suspensions exhibit instabilities, and our results generalize the long-wave predictions of Simha and Ramaswamy²⁷ on aligned suspensions. In Sec. IV, we complement and expand upon the results from the linear stability analysis by performing nonlinear simulations in two dimensions. This allows us to investigate the long-time evolution of the suspensions and the pattern formation for the instabilities, as well as their relation to fluid mixing. In particular, we find that the dynamics in suspensions of pushers result in very efficient mixing, which we quantify using a multiscale mixing norm.

II. KINETIC MODEL

A. Governing equations

We represent the configuration of a suspension of rodlike particles by means of a distribution function⁴¹ $\Psi(\mathbf{x}, \mathbf{p}, t)$ of the particle position \mathbf{x} and director \mathbf{p} , where \mathbf{p} is a unit vector defining the particle orientation and direction. The evolution of the suspension is described by a conservation equation,

$$\frac{\partial \Psi}{\partial t} = -\nabla_{\mathbf{x}} \cdot (\dot{\mathbf{x}}\Psi) - \nabla_{\mathbf{p}} \cdot (\dot{\mathbf{p}}\Psi), \quad (1)$$

where $\nabla_{\mathbf{p}}$ denotes the gradient operator on the unit sphere. The distribution function is normalized as follows:

$$\frac{1}{V} \int_V d\mathbf{x} \int_S d\mathbf{p} \Psi(\mathbf{x}, \mathbf{p}, t) = n, \quad (2)$$

where V is volume of the region of interest, n is the mean number density of particles in the suspension, and S is the surface of the unit sphere. We also define the linear system size as $L = V^{1/3}$.

The conservation equation (1) involves flux velocities in \mathbf{x} and \mathbf{p} , which for rodlike particles swimming at a velocity $U_0\mathbf{p}$ relative to a background flow can be modeled as

$$\dot{\mathbf{x}} = U_0\mathbf{p} + \mathbf{u} - D\nabla_{\mathbf{x}}(\ln \Psi), \quad (3)$$

$$\dot{\mathbf{p}} = (\mathbf{I} - \mathbf{p}\mathbf{p}) \cdot [(\gamma\mathbf{E} + \mathbf{W}) \cdot \mathbf{p} - d_r\nabla_{\mathbf{p}}(\ln \Psi)]. \quad (4)$$

In Eq. (3), the translational velocity of a particle is represented as the sum of its swimming velocity $U_0\mathbf{p}$ with orientation \mathbf{p} and of the local fluid velocity $\mathbf{u}(\mathbf{x}, t)$ induced by the other particles in the suspension. We also model diffusion through an isotropic translational diffusion coefficient D . This may represent the effects of small-scale hydrodynamic fluctuations (hydrodynamic dispersion) or of particle tumbling. In a more general model, D may be assumed to depend on the director \mathbf{p} . Similarly, the angular velocity in Eq. (4) arises from the local linear flow and is modeled using

Jeffery's equation^{42,43} in terms of the fluid rate-of-strain tensor $\mathbf{E}=(\nabla\mathbf{u}+\nabla\mathbf{u}^\dagger)/2$ and vorticity tensor $\mathbf{W}=(\nabla\mathbf{u}-\nabla\mathbf{u}^\dagger)/2$ and of a shape parameter $-1\leq\gamma\leq 1$ [for a spheroidal particle, $\gamma=(A^2-1)/(A^2+1)$, where A is the particle aspect ratio, and for a slender rod $\gamma\approx 1$]. Angular diffusion is included through the rotary diffusion coefficient d_r . Note that in the present formulation, the two coefficients for translational and rotary diffusion are assumed to be independent for simplicity: This is not generally the case in suspensions of swimming particles, where the hydrodynamic translational diffusivity may be shown to be inversely proportional to the rotary diffusivity.¹⁸

To close the equations, the velocity $\mathbf{u}(\mathbf{x},t)$ of the fluid must be determined. In the low-Reynolds-number limit of interest here, it satisfies the momentum and mass conservation equations,

$$-\mu\nabla_{\mathbf{x}}^2\mathbf{u}+\nabla_{\mathbf{x}}q=\nabla_{\mathbf{x}}\cdot\Sigma^p, \quad \nabla_{\mathbf{x}}\cdot\mathbf{u}=0, \quad (5)$$

where μ denotes the viscosity of the suspending fluid and q is the fluid pressure. The fluid motion arises from the active particle stress $\Sigma^p(\mathbf{x},t)$ given by

$$\Sigma^p(\mathbf{x},t)=\sigma_0\int_S\Psi(\mathbf{x},\mathbf{p},t)\left(\mathbf{p}\mathbf{p}-\frac{\mathbf{I}}{3}\right)d\mathbf{p}. \quad (6)$$

This expression can be derived based on Kirkwood theory.⁴¹ In particular, Σ^p can be viewed as a configuration average over all orientations \mathbf{p} of the force dipoles (or stresslets) $\sigma_0(\mathbf{p}\mathbf{p}-\mathbf{I}/3)$ exerted by the particles on the fluid (see Batchelor⁴⁴); it may also be interpreted as a local nematic order parameter weighted by the particle concentration. It can be shown that the stresslet strength σ_0 arises from the first moment of the force distribution on the particle surface.¹⁸ In Eq. (6), we neglect the contribution of the stresslet from particle interactions and only retain the lowest-order contribution from the single-particle swimming. In this case, σ_0 can be shown from the micromechanics of swimming to be related to the swimming velocity U_0 by a relation of the type^{18,27}

$$\frac{\sigma_0}{U_0\mu l^2}=\alpha, \quad (7)$$

where l is the characteristic dimension of the particles and α is a dimensionless $O(1)$ constant which depends on the precise swimming mechanism. Note that the sign of σ_0 (and therefore α) may be either positive or negative depending on the swimming mechanism. A particle which propels itself by exerting a force near its tail (pusher) will result in $\sigma_0<0$ (and $\alpha<0$), whereas a particle that propels itself using its head (puller) will result in $\sigma_0>0$ ($\alpha>0$).^{16,18,27} In the following, we consider both cases but will focus on the case of pushers ($\sigma_0<0$), which is more common in nature and also results in more interesting dynamics.

In addition to the distribution function $\Psi(\mathbf{x},\mathbf{p},t)$, it is useful to define a local concentration field $c(\mathbf{x},t)$ and a local particle director field $\mathbf{n}(\mathbf{x},t)$ as follows:

$$c(\mathbf{x},t)=\int_S\Psi(\mathbf{x},\mathbf{p},t)d\mathbf{p}, \quad (8)$$

$$\mathbf{n}(\mathbf{x},t)=\frac{1}{c(\mathbf{x},t)}\int_S\mathbf{p}\Psi(\mathbf{x},\mathbf{p},t)d\mathbf{p}. \quad (9)$$

Upon integration of the conservation equation (1) over \mathbf{p} , and using Eq. (3) for the flux velocity $\dot{\mathbf{x}}$, it can be shown that the concentration field $c(\mathbf{x},t)$ satisfies the following evolution equation:

$$\frac{\partial c}{\partial t}+\nabla_{\mathbf{x}}\cdot[(U_0\mathbf{n}+\mathbf{u})c]-D\nabla_{\mathbf{x}}^2c=0, \quad (10)$$

or equivalently, making use of the incompressibility condition $\nabla_{\mathbf{x}}\cdot\mathbf{u}=0$,

$$\frac{\partial c}{\partial t}+\mathbf{u}\cdot\nabla_{\mathbf{x}}c-D\nabla_{\mathbf{x}}^2c=-U_0\nabla_{\mathbf{x}}\cdot(c\mathbf{n}). \quad (11)$$

In particular, Eq. (11) identifies $-U_0\nabla_{\mathbf{x}}\cdot(c\mathbf{n})$ as a source term for magnitude changes in the concentration field c , which is otherwise advected by the fluid velocity \mathbf{u} and smoothed by translational diffusion.

B. Nondimensionalization

The governing equations are made dimensionless using the following characteristic velocity, length, and time scales:

$$u_c=U_0, \quad l_c=(nl^2)^{-1}, \quad t_c=l_c/u_c. \quad (12)$$

Note that $l_c=(V/V_p)l$, where $V_p=Nl^3$ is the effective volume taken up by the swimming particles (if N is the total number of particles in volume V). This choice of characteristic scales eliminates all parameters from the equations except for the $O(1)$ constant α and shape parameter γ , as well as dimensionless translational and rotary diffusion coefficients. Further, the number density n now appears in the equations only through the normalized system size, L/l_c . The conservation equation (1) remains unchanged with the distribution function now normalized as

$$\frac{1}{V}\int_V d\mathbf{x}\int_S d\mathbf{p}\Psi(\mathbf{x},\mathbf{p},t)=1, \quad (13)$$

where now $V=(L/l_c)^3$ and Ψ has conserved mean $1/4\pi$. After nondimensionalization, the flux velocities become

$$\dot{\mathbf{x}}=\mathbf{p}+\mathbf{u}-D\nabla_{\mathbf{x}}(\ln\Psi), \quad (14)$$

$$\dot{\mathbf{p}}=(\mathbf{I}-\mathbf{p}\mathbf{p})\cdot[(\gamma\mathbf{E}+\mathbf{W})\cdot\mathbf{p}-d_r\nabla_{\mathbf{p}}(\ln\Psi)], \quad (15)$$

where the diffusion coefficients D and d_r are now dimensionless. Finally, the momentum and continuity equations simplify as

$$-\nabla_{\mathbf{x}}^2\mathbf{u}+\nabla_{\mathbf{x}}q=\nabla_{\mathbf{x}}\cdot\Sigma^p, \quad \nabla_{\mathbf{x}}\cdot\mathbf{u}=0, \quad (16)$$

with the following dimensionless particle stress:

$$\Sigma^p(\mathbf{x},t)=\alpha\int_S\Psi(\mathbf{x},\mathbf{p},t)\left(\mathbf{p}\mathbf{p}-\frac{\mathbf{I}}{3}\right)d\mathbf{p}. \quad (17)$$

C. The system entropy

The total entropy

$$\mathcal{S} = \int_V d\mathbf{x} \int_S d\mathbf{p} \frac{\Psi}{\Psi_0} \ln \left(\frac{\Psi}{\Psi_0} \right), \quad (18)$$

where $\Psi_0 = 1/4\pi$, plays the role of a system energy. Note that $\mathcal{S} \geq 0$ and realizes its minimum value of zero only for $\Psi \equiv \Psi_0$, that is, for the homogeneous and isotropic state. Working only with the conservation equation (1), one obtains after some algebra

$$4\pi\dot{\mathcal{S}} = \frac{3\gamma}{\alpha} \int_V d\mathbf{x} \mathbf{E} : \Sigma^p - \int_V d\mathbf{x} \int_S d\mathbf{p} [D|\nabla_{\mathbf{x}} \ln \Psi|^2 + d_r |\nabla_{\mathbf{p}} \ln \Psi|^2] \Psi. \quad (19)$$

The latter terms on the right-hand side plainly arise from diffusive processes, while the first term arises from the flux term $\nabla_{\mathbf{p}} \cdot (\mathbf{p}\Psi)$, where use has been made of the identity

$$\nabla_{\mathbf{p}} \cdot [(\mathbf{I} - \mathbf{p}\mathbf{p}) \cdot (\gamma\mathbf{E} + \mathbf{W}) \cdot \mathbf{p}] = -3\gamma\mathbf{p}\mathbf{p} : \mathbf{E}, \quad (20)$$

the expression (17) for Σ^p , and fluid incompressibility. This first right-hand term in Eq. (19) is proportional to the active input power generated by the particles as they propel themselves through the fluid and is of definite sign. The momentum equation (16) can be recast as

$$\nabla_{\mathbf{x}} \cdot (q\mathbf{I} - 2\mathbf{E}) = \nabla_{\mathbf{x}} \cdot \Sigma^p. \quad (21)$$

Taking the dot product of Eq. (21) with \mathbf{u} , integrating over the fluid domain V , yields the identity

$$\int_V 2\mathbf{E} : \mathbf{E} d\mathbf{x} = - \int_V \mathbf{E} : \Sigma^p d\mathbf{x}, \quad (22)$$

where use is made of integration by parts, fluid incompressibility, and symmetry of \mathbf{E} . The left-hand side in Eq. (22) is the rate of viscous dissipation in the fluid and is balanced by the active input power. Hence,

$$4\pi\dot{\mathcal{S}} = - \frac{6\gamma}{\alpha} \int_V d\mathbf{x} \mathbf{E} : \mathbf{E} - \int_V d\mathbf{x} \int_S d\mathbf{p} [D|\nabla_{\mathbf{x}} \ln \Psi|^2 + d_r |\nabla_{\mathbf{p}} \ln \Psi|^2] \Psi. \quad (23)$$

Note that for $\alpha > 0$, the entropy is driven down by both diffusive processes and by the positive definiteness of the rate of viscous dissipation term. Hence, for suspensions of pullers, where $\alpha > 0$, and in the absence of any external forcing or boundary effects, fluctuations from the isotropic state as measured by the entropy are expected to monotonically dissipate. This expectation is borne out by the results of our linear stability analysis of the isotropic state, as well as by the results of our nonlinear simulations, both given below.

For suspension of pushers, where $\alpha < 0$, the situation is entirely different as the leading term now enters with a positive sign and suggests a feedback loop wherein fluctuations create velocity gradients which increase fluctuations (as measured by the entropy), with this process only limited, and eventually balanced, by the diffusive processes in the system. Again, this picture seems borne out by our results below.

The derivation of Eq. (23) also makes clear that the source of instability in this system lies not in the presence of the propulsive term \mathbf{p} in the center of mass flux [i.e., in Eq. (3)], but rather in the sign, through negative α , of the force dipoles induced by the swimmers. The Doi model for dilute suspensions of rigid rods⁴¹ is essentially identical to our model here, although obviously lacking the additional swimmer flux term and has an extra stress term identical to ours but with a positive α , which arises through calculating the extra stress induced by thermodynamic fluctuations of the rods rather than from self-propulsion (see Otto and Tzavaras⁴⁵ for use of system entropy in analyzing the smoothness of solutions to Doi's rod suspension theory).

D. Reduced equations for locally aligned case

In the case where a single particle director exists at a given location \mathbf{x} , and when particle diffusion can be neglected ($D=0$, $d_r \equiv 0$), a set of reduced equations for the local concentration and director field can be derived. More specifically, consider a distribution function in the form $\Psi(\mathbf{x}, \mathbf{p}, t) = c(\mathbf{x}, t) \delta[\mathbf{p} - \mathbf{n}(\mathbf{x}, t)]$, where δ denotes the Dirac delta function.

In this case, the fluid velocity still satisfies Eq. (16), with the particle stress tensor

$$\Sigma^p(\mathbf{x}, t) = \alpha c(\mathbf{x}, t) \left(\mathbf{nn} - \frac{\mathbf{I}}{3} \right). \quad (24)$$

Equation (10) for the evolution of the concentration field simplifies directly to

$$\frac{\partial c}{\partial t} + \nabla_{\mathbf{x}} \cdot [(\mathbf{n} + \mathbf{u})c] = 0. \quad (25)$$

In addition, we can also obtain an equation for \mathbf{n} by multiplying Eq. (1) by \mathbf{p} and integrating over \mathbf{p} . This yields

$$\frac{\partial}{\partial t} (\mathbf{n}c) = - \nabla_{\mathbf{x}} \cdot [(\mathbf{n} + \mathbf{u})\mathbf{n}c] + c(\mathbf{I} - \mathbf{nn}) \cdot (\gamma\mathbf{E} + \mathbf{W}) \cdot \mathbf{n}, \quad (26)$$

where we made use of Eq. (15) for the angular flux velocity and of the integration by parts formula

$$\int_S \mathbf{p} \nabla_{\mathbf{p}} \cdot (\mathbf{p}\Psi) d\mathbf{p} = - \int_S \mathbf{p}\Psi d\mathbf{p}. \quad (27)$$

Expanding the derivatives in Eq. (26) and using Eq. (25) to eliminate c , we find the evolution equation for the director field,

$$\frac{\partial \mathbf{n}}{\partial t} = - (\mathbf{n} + \mathbf{u}) \cdot \nabla_{\mathbf{x}} \mathbf{n} + (\mathbf{I} - \mathbf{nn}) \cdot (\gamma\mathbf{E} + \mathbf{W}) \cdot \mathbf{n}. \quad (28)$$

To summarize, the evolution of the concentration and director fields in a suspension of locally aligned particles, in which diffusion is negligible, is determined by Eqs. (25) and (28), in which the fluid velocity satisfies Eq. (16) with the simplified expression (24) for the active particle stress.

III. LINEAR STABILITY ANALYSES

A. Nearly aligned suspension

We first analyze the linear stability of a nearly aligned suspension using the reduced equations of Sec. II D. We consider a nearly uniform suspension in which the particles are all nearly aligned along the \hat{z} -direction: $c(\mathbf{x}, t) = 1 + \epsilon c'(\mathbf{x}, t)$, $\mathbf{n}(\mathbf{x}, t) = \hat{z} + \epsilon \mathbf{n}'(\mathbf{x}, t)$, where $\mathbf{n}' \cdot \hat{z} = 0$ (which ensures that the length of \mathbf{n} remains 1 to order ϵ^2 for $|\epsilon| \ll 1$). Define also the perturbation fluid velocity and pressure fields: $\mathbf{u}(\mathbf{x}) = \epsilon \mathbf{u}'(\mathbf{x})$ and $q(\mathbf{x}) = \epsilon q'(\mathbf{x})$, respectively. We will determine the evolution of the perturbation variables c' and \mathbf{n}' in the limit where $|\epsilon| \ll 1$.

Expanding Eqs. (25) and (28) and retaining terms of order ϵ , we find

$$\frac{\partial c'}{\partial t} + \hat{z} \cdot \nabla_{\mathbf{x}} c' + \nabla_{\mathbf{x}} \cdot \mathbf{n}' = 0, \quad (29)$$

$$\frac{\partial \mathbf{n}'}{\partial t} + \hat{z} \cdot \nabla_{\mathbf{x}} \mathbf{n}' = (\mathbf{I} - \hat{z}\hat{z}) \cdot (\gamma \mathbf{E}' + \mathbf{W}') \cdot \hat{z}. \quad (30)$$

The momentum and continuity equations for the fluid velocity field become

$$-\nabla^2 \mathbf{u}' + \nabla_{\mathbf{x}} q' = \alpha \nabla_{\mathbf{x}} \cdot (\mathbf{n}' \hat{z} + \hat{z} \mathbf{n}' + c' \hat{z}\hat{z}), \quad (31)$$

$$\nabla_{\mathbf{x}} \cdot \mathbf{u}' = 0. \quad (32)$$

We seek solutions written as plane waves with wave vector \mathbf{k} , $c'(\mathbf{x}, t) = \tilde{c}(\mathbf{k}) \exp(i\mathbf{k} \cdot \mathbf{x} + \sigma t)$, with similar expressions for all the other perturbation variables. Equations (31) and (32) can be solved by Fourier transform for the coefficient $\tilde{\mathbf{u}}(\mathbf{k})$ of the fluid velocity as

$$\tilde{\mathbf{u}}(\mathbf{k}) = \frac{i\alpha}{k^2} (\mathbf{I} - \hat{\mathbf{k}}\hat{\mathbf{k}}) \cdot (\tilde{\mathbf{n}}\hat{z} + \hat{z}\tilde{\mathbf{n}} + \tilde{c}\hat{z}\hat{z}) \cdot \mathbf{k}, \quad (33)$$

where $k = |\mathbf{k}|$ and $\hat{\mathbf{k}} = \mathbf{k}/k$. The rate-of-strain and vorticity tensors are then easily obtained as

$$\tilde{\mathbf{E}} = \frac{i}{2} (\tilde{\mathbf{u}}\mathbf{k} + \mathbf{k}\tilde{\mathbf{u}}), \quad \tilde{\mathbf{W}} = \frac{i}{2} (\tilde{\mathbf{u}}\mathbf{k} - \mathbf{k}\tilde{\mathbf{u}}). \quad (34)$$

From Eq. (33), it can be seen that only the components of the wave vector that lie in the $(\hat{z}, \tilde{\mathbf{n}})$ plane will result in a nonzero velocity. Without loss of generality, we can therefore assume that \mathbf{k} lies in this plane and define θ as the angle between \mathbf{k} and \hat{z} : $\mathbf{k} = k(\cos \theta \hat{z} + \sin \theta \tilde{\mathbf{n}}/\tilde{n})$ (where $\tilde{n} = |\tilde{\mathbf{n}}|$). With these notations, and after substitution of Eq. (34) into the linearized equations (29) and (30), we arrive at

$$\lambda \tilde{c} = -ik \sin \theta \tilde{n}, \quad (35)$$

$$\lambda \tilde{n} = -\frac{\alpha}{2} [(\gamma + 1) \cos^2 \theta - (\gamma - 1) \sin^2 \theta] \times (\cos 2\theta \tilde{n} - \sin \theta \cos \theta \tilde{c}), \quad (36)$$

where we have defined $\lambda = \sigma + ik \cos \theta$. This is an eigenvalue problem for the variable λ , the solution for which is obtained as

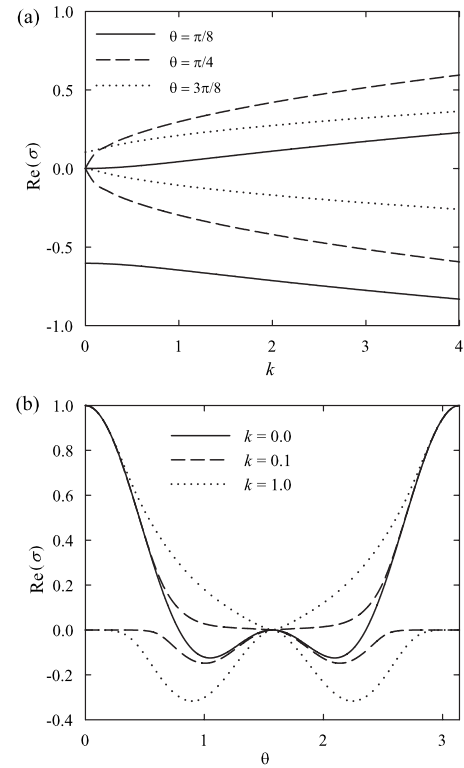


FIG. 1. Growth rates $\text{Re}(\sigma)$ in a suspension of nearly aligned swimming particles as function of (a) the wavevector k for various wave angles and (b) the wave angle θ for various wavenumbers, obtained from Eq. (37). Reproduced with permission from Ref. 28.

$$\lambda_{\pm} = \frac{1}{2} f(\theta) \cos 2\theta \left\{ 1 \pm \left[1 + 4ik \frac{\sin^2 \theta \cos \theta}{f(\theta) \cos^2 2\theta} \right]^{1/2} \right\}, \quad (37)$$

where $f(\theta) = -\alpha[(\gamma + 1) \cos^2 \theta - (\gamma - 1) \sin^2 \theta]/2$. The growth rate, or real part of λ , is plotted as a function of the wave-number k in Fig. 1 for a variety of wave angles θ and for the choice of parameters $\alpha = -1$, $\gamma = 1$ [the case $\alpha = +1$ is obtained by simply changing the sign of $\text{Re}(\lambda)$].

For $k > 0$ the two growth rates have opposite signs. This means that there is always a positive growth rate, i.e., suspensions of aligned particles are always unstable to density and orientation perturbations. This is consistent with particle simulations, which show an instability for all wave angles θ and wave numbers k .¹⁸ In the long-wave limit ($k \rightarrow 0$), the two eigenvalues become

$$\lambda_+ = f(\theta) \cos 2\theta, \quad \lambda_- = 0. \quad (38)$$

The first eigenvalue is that previously obtained by Simha and Ramaswamy,²⁷ who concluded that only certain ranges of wave angles were subject to an instability. The nature of their analysis misses the k -dependence and, in particular, the fact that for $k > 0$ the second eigenvalue λ_- becomes nonzero (and oppositely signed as well). Note that this additional eigenvalue has also been found by Pedley.⁴⁶ At high wavenumbers, our theory predicts an increase in growth rate with k : In a real system, however, one should expect diffusion to stabilize and damp high-wavenumber fluctuations.

B. Nearly isotropic suspension

1. Eigenvalue problem

We now consider the stability of a nearly uniform and isotropic suspension, for which the distribution function can be written as

$$\Psi(\mathbf{x}, \mathbf{p}, t) = \frac{1}{4\pi} [1 + \epsilon \Psi'(\mathbf{x}, \mathbf{p}, t)], \quad (39)$$

with $|\epsilon| \ll 1$. For simplicity, we neglect angular diffusion ($d_r = 0$), as including it would significantly complicate the analysis, but we retain translational diffusion. Substituting Eq. (39) into Eq. (1) and linearizing lead to

$$\frac{\partial \Psi'}{\partial t} = -\mathbf{p} \cdot \nabla_{\mathbf{x}} \Psi' + D \nabla_{\mathbf{x}}^2 \Psi' + 3\gamma \mathbf{p} \mathbf{p} : \mathbf{E}', \quad (40)$$

where we have used Eqs. (14) and (15) for the flux velocities as well as the antisymmetric property of the vorticity tensor. The momentum and continuity equations (16) for the fluid motion also apply for the perturbation variables, with the following stress tensor:

$$\Sigma'^p(\mathbf{x}, t) = \frac{\alpha}{4\pi} \int_S \Psi'(\mathbf{x}, \mathbf{p}, t) \left(\mathbf{p} \mathbf{p} - \frac{\mathbf{I}}{3} \right) d\mathbf{p}. \quad (41)$$

Once again, we consider a plane wave perturbation for the distribution function, $\Psi'(\mathbf{x}, \mathbf{p}, t) = \tilde{\Psi}(\mathbf{p}, \mathbf{k}) \exp(i\mathbf{k} \cdot \mathbf{x} + \sigma t)$, and for all other perturbation variables. We solve for the Fourier amplitude $\tilde{\mathbf{u}}(\mathbf{k})$ of the fluid velocity as

$$\tilde{\mathbf{u}} = \frac{i}{k} (\mathbf{I} - \hat{\mathbf{k}} \hat{\mathbf{k}}) \cdot \tilde{\Sigma}^p \cdot \hat{\mathbf{k}}, \quad (42)$$

and the rate-of-strain tensor is inferred as

$$\tilde{\mathbf{E}} = \frac{i}{2} (\tilde{\mathbf{u}} \mathbf{k} + \mathbf{k} \tilde{\mathbf{u}}). \quad (43)$$

Equations (40), (42), and (43) can be combined to yield an expression for $\tilde{\Psi}(\mathbf{k}, \mathbf{p})$. After some algebra, we find

$$\tilde{\Psi} = \frac{-3\gamma(\hat{\mathbf{k}} \cdot \mathbf{p})}{\sigma + k^2 D + i\mathbf{k} \cdot \mathbf{p}} \mathbf{p} \cdot (\mathbf{I} - \hat{\mathbf{k}} \hat{\mathbf{k}}) \cdot \tilde{\Sigma}^p \cdot \hat{\mathbf{k}}. \quad (44)$$

Recalling the definition of the active stress $\tilde{\Sigma}^p$, this may also be written as

$$\tilde{\Psi} = -\frac{3\alpha\gamma}{4\pi} \frac{(\hat{\mathbf{k}} \cdot \mathbf{p})}{\sigma + k^2 D + i\mathbf{k} \cdot \mathbf{p}} \mathbf{p} \cdot \mathbf{F}(\tilde{\Psi}), \quad (45)$$

where we have defined the operator \mathbf{F} as

$$\mathbf{F}(\tilde{\Psi}) = (\mathbf{I} - \hat{\mathbf{k}} \hat{\mathbf{k}}) \cdot \int_S \mathbf{p}' (\mathbf{p}' \cdot \hat{\mathbf{k}}) \tilde{\Psi} d\mathbf{p}'. \quad (46)$$

To obtain an eigenvalue relation, apply \mathbf{F} to both sides of Eq. (45) to yield

$$\mathbf{F}(\tilde{\Psi}) = -\frac{3\alpha\gamma}{4\pi} \int_S \frac{(\hat{\mathbf{k}} \cdot \mathbf{p})^2}{\sigma + k^2 D + i\mathbf{k} \cdot \mathbf{p}} (\mathbf{I} - \hat{\mathbf{k}} \hat{\mathbf{k}}) \cdot \mathbf{p} \times \mathbf{p} \cdot \mathbf{F}(\tilde{\Psi}) d\mathbf{p}. \quad (47)$$

Observe that Eq. (47) is invariant under rotation, so that without loss of generality we can choose a coordinate system such that $\hat{\mathbf{k}} = \hat{\mathbf{z}}$. In spherical coordinates with polar axis $\hat{\mathbf{k}}$, we have $\mathbf{p} = [\sin \theta \cos \phi, \sin \theta \sin \phi, \cos \theta]$ and $d\mathbf{p} = \sin \theta d\theta d\phi$ with $\phi \in [0, 2\pi)$ and $\theta \in [0, \pi]$. With these notations, Eq. (47) becomes

$$\mathbf{F}(\tilde{\Psi}) = -\frac{3\alpha\gamma}{4\pi} \int_0^\pi \frac{\cos^2 \theta \sin^3 \theta}{\sigma + k^2 D + ik \cos \theta} d\theta \times \int_0^{2\pi} (\cos^2 \phi \hat{\mathbf{x}} \hat{\mathbf{x}} + \sin^2 \phi \hat{\mathbf{y}} \hat{\mathbf{y}}) \cdot \mathbf{F}(\tilde{\Psi}) d\phi. \quad (48)$$

Performing the integral over ϕ and using the fact that $\mathbf{F}(\tilde{\Psi})$ lies in the $\hat{\mathbf{x}}\text{-}\hat{\mathbf{y}}$ plane [cf. Eq. (46)], we obtain

$$\mathbf{F}(\tilde{\Psi}) = -\frac{3\alpha\gamma}{4} \int_0^\pi \frac{\cos^2 \theta \sin^3 \theta}{\sigma + k^2 D + ik \cos \theta} d\theta \mathbf{F}(\tilde{\Psi}), \quad (49)$$

from which the dispersion relation is inferred as

$$-\frac{3\alpha\gamma}{4} \int_0^\pi \frac{\cos^2 \theta \sin^3 \theta}{\sigma + k^2 D + ik \cos \theta} d\theta = 1. \quad (50)$$

The integral over θ in Eq. (50) may also be performed analytically, yielding

$$\frac{3i\alpha\gamma}{4k} \left[2a^3 - \frac{4}{3}a + (a^4 - a^2) \log \left(\frac{a-1}{a+1} \right) \right] = 1, \quad (51)$$

where we have defined $a = -i(\sigma + Dk^2)/k$.

2. Eigenmodes

The above analysis shows that the only requirement on the vector $\mathbf{F}(\tilde{\Psi})$ is that it lie in the $\hat{\mathbf{x}}\text{-}\hat{\mathbf{y}}$ plane, i.e., that it is perpendicular to $\hat{\mathbf{k}}$. Using Eq. (45), we therefore find that the eigenmodes for the distribution function are of the form

$$\tilde{\Psi}(\mathbf{k}, \mathbf{p}) = \frac{(\hat{\mathbf{k}} \cdot \mathbf{p})(\hat{\mathbf{k}}_\perp \cdot \mathbf{p})}{\sigma + k^2 D + i\mathbf{k} \cdot \mathbf{p}}, \quad (52)$$

where $\hat{\mathbf{k}}_\perp$ is any unit vector perpendicular to $\hat{\mathbf{k}}$. The spatial variations in the distribution function are then obtained as $\Psi'(\mathbf{x}, \mathbf{p}, t) = \tilde{\Psi}(\mathbf{k}, \mathbf{p}) \exp(i\mathbf{k} \cdot \mathbf{x} + \sigma t)$. It should be noted that the eigenmodes (52) are not a complete basis for fluctuations in \mathbf{p} , as can be seen, for instance, since $\tilde{\Psi}(\mathbf{k}, \mathbf{p})$ only includes the first harmonic in the azimuthal angle ϕ . Therefore, not every linear perturbation in the distribution function can be decomposed as superposition of eigenmodes, even when an eigenvalue exists.

An interesting property of Eq. (52) is that its corresponding concentration field is uniform in space,

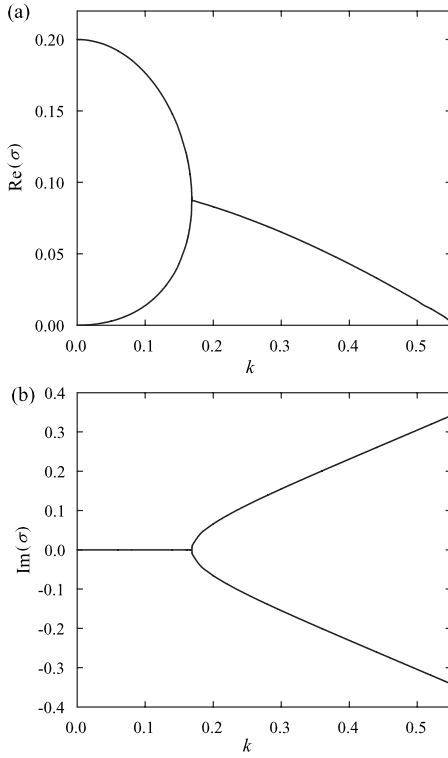


FIG. 2. (a) Real part $\text{Re}(\sigma)$ and (b) imaginary part $\text{Im}(\sigma)$ of the complex growth rate σ as a function of the wavenumber k in a nearly isotropic suspension of active particles, in the case $\alpha=-1$, $\gamma=1$, and $D=0$ (no diffusion), obtained by numerically solving the dispersion relation (51). Reproduced with permission from Ref. 28.

$$c'(\mathbf{x}, t) = \int_S \Psi'(\mathbf{x}, \mathbf{p}, t) d\mathbf{p} = 0, \quad (53)$$

i.e., the linear stability analysis does not predict the growth of any concentration fluctuations. We will see, however, in Sec. IV that concentration fluctuations do occur as a result of nonlinearities. The corresponding stress tensor, however, is nonzero. Substituting Eq. (52) into the definition of the active particle stress easily shows, by making use of the dispersion relation, Eq. (50), that the active stress eigenmodes are shear stresses of the form

$$\bar{\Sigma}^p = \hat{\mathbf{k}}\hat{\mathbf{k}}_{\perp} + \hat{\mathbf{k}}_{\perp}\hat{\mathbf{k}}. \quad (54)$$

3. Solution of the dispersion relation

The dispersion relation (51), in which $a = -i(\sigma + Dk^2)/k$, can be solved numerically for $\sigma(k)$ for various choices of the parameters α , γ , and D . The solution for $\alpha=-1$, $\gamma=1$, and $D=0$ (no diffusion) is shown in Fig. 2, where the real and imaginary parts of σ are plotted versus k . In particular, we observe that at low wavenumbers, $\text{Re}(\sigma) > 0$ (positive growth rate), and $\text{Im}(\sigma) \equiv 0$, which suggests that low-wavenumber shear stress fluctuations will amplify exponentially in suspensions of pushers. At higher wavenumbers (above $k \approx 0.17$), $\text{Im}(\sigma)$ becomes positive, showing that stress oscillations will occur and amplify. At wavenumber $k \approx 0.55$, $\text{Re}(\sigma)$ becomes zero; beyond this value, the dynamics are no longer described by an eigenfunction, and the

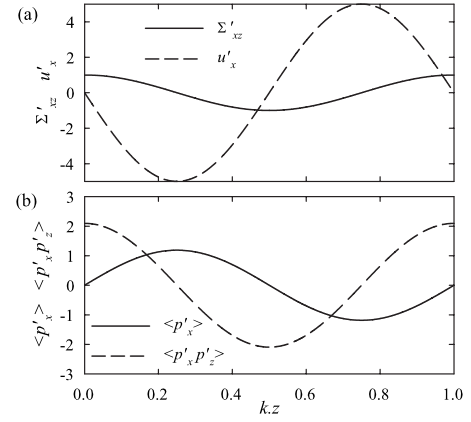


FIG. 3. Unstable eigenmode for a nearly isotropic suspension of pushers ($\alpha=-1$, $\gamma=1$) for wavevector $\mathbf{k}=0.2\hat{\mathbf{z}}$: (a) perturbation shear stress $\Sigma'_{xz}(z)$ and disturbance velocity $u'_x(z)$; (b) first and second moments of the distribution function with respect to the director field, $\langle p'_x \rangle$ and $\langle p'_x p'_z \rangle$.

stress fluctuations become damped.⁴⁷ Including translational diffusion ($D > 0$) simply shifts the solution for $\text{Re}(\sigma)$ by $-Dk^2$, which results in a more rapid damping of the instability at high wavenumbers; low wavenumbers, however, always remain unstable. Rotational diffusion, which is not included in the present theory, can also be shown to have a damping effect and may, in fact, stabilize even low-wavenumber fluctuations.⁴⁷ In the case of pullers ($\alpha > 0$), the sign of $\text{Re}(\sigma)$ changes in Fig. 2(a), which suggests that no instability takes place in that case: This fact is confirmed in numerical simulations, as we discuss in Sec. IV.

Insight into the long-wave behavior can be obtained by seeking an asymptotic solution for $\sigma(k)$. Expanding the dispersion relation for $|k| \ll 1$, we arrive at an algebraic equation for $\sigma(k)$,

$$\sigma^3 + \frac{\alpha\gamma}{5}\sigma^2 + \frac{\alpha\gamma Dk^2}{5}\sigma - \frac{3\alpha\gamma k^2}{35} + O(k^3) = 0. \quad (55)$$

We seek a solution in the form: $\sigma = \sigma_0 + \sigma_2 k^2 + O(k^3)$. Substituting this expansion into Eq. (55), expanding to $O(k^2)$, and identifying powers of k , we can solve for σ_0 and σ_2 as

$$\sigma_0 = -\frac{\alpha\gamma}{5}, \quad (56)$$

$$\sigma_2 = -D + \frac{15}{7}(\alpha\gamma)^{-1}, \quad (57)$$

from which we infer the long-wave solution of Eq. (51),

$$\sigma = -\frac{\alpha\gamma}{5} + \left[\frac{15}{7}(\alpha\gamma)^{-1} - D \right] k^2 + O(k^3). \quad (58)$$

As expected, we find that σ is real at low wavenumbers and that $\text{Re}(\sigma) > 0$ for $\alpha < 0$. We also find that $\text{Re}(\sigma)$ decreases quadratically for small k , in particular, as a result of translational diffusion.

A full eigenmode for this system, obtained for $\hat{\mathbf{k}} = \hat{\mathbf{z}}$ and $\hat{\mathbf{k}}_{\perp} = \hat{\mathbf{x}}$ and calculated using Eq. (52) and the numerical solution of the dispersion relation, is illustrated in Figs. 3 and 4. Figure 3 shows the perturbation shear stress Σ'_{xz} and velocity $\mathbf{u}'(\mathbf{x}, t) = u'_x(z)\hat{\mathbf{x}}$, as well as the first and second moments of

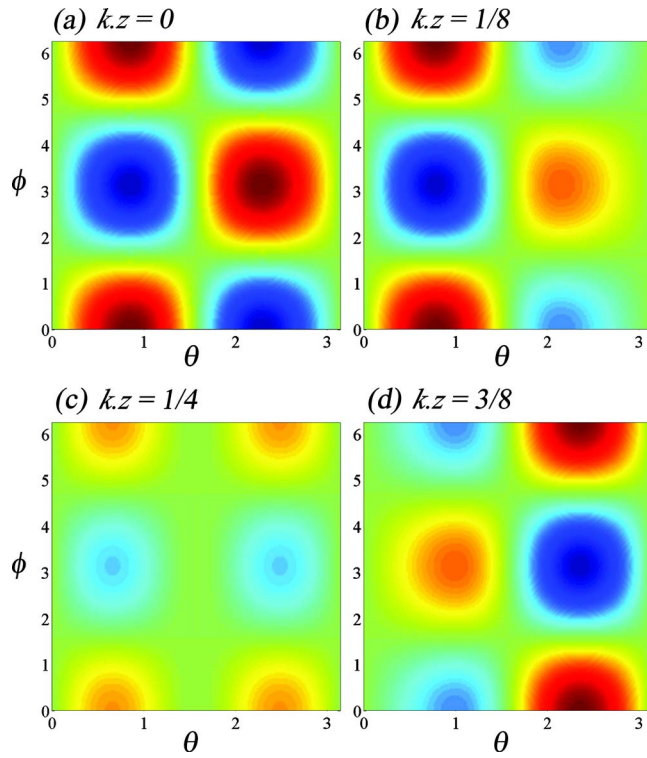


FIG. 4. (Color online) Unstable eigenmode for the distribution function Ψ for a nearly isotropic suspension of pushers ($\alpha=-1$, $\gamma=1$) for wavevector $\mathbf{k}=0.2\hat{z}$: orientation distributions at various positions z in the wave direction, where the angles θ and ϕ are defined by: $\mathbf{p} = [\sin \theta \cos \phi, \sin \theta \sin \phi, \cos \theta]$.

the distribution function with respect to the director fields, $\langle p'_x \rangle$ and $\langle p'_z \rangle$. The full distribution function at various values of $kz = \mathbf{k} \cdot \mathbf{x}$, within a given wavelength, is shown in Fig. 4.

IV. NONLINEAR SIMULATIONS

A. Simulation method

In this section, we perform numerical simulations of the kinetic equations of Sec. II to investigate the long-time evolution of the suspensions. In three dimensions, the kinetic model involves five configuration variables (three spatial variables and two angles), rendering simulation intractable. We therefore restrict our attention to two-dimensional periodic systems, in which the particles are constrained to move and rotate only in the (x, y) -plane with direction parametrized by an angle $\phi \in [0, 2\pi)$, and for which the distribution function Ψ is invariant along the z -direction: $\Psi(\mathbf{x}, \mathbf{p}, t) = \Psi(x, y, \phi, t)$ (in particular, $\mathbf{p} = [\cos \phi, \sin \phi, 0]$).

In this case the governing equations are easily integrated as follows. The fluid flow equations (16) are solved spectrally using the fast Fourier transform algorithm by expanding the flow variables in Fourier series and truncating the series after a finite number of modes (128–256 modes in each spatial direction were used in the simulations presented here). Once the fluid velocity is known, the conservation equation (1) for the distribution function can be integrated in time using second-order finite differences for the flux terms and a second-order Adams–Bashforth time-marching

scheme. Translational and angular diffusions are included in all simulations to ensure that the distribution function remains bounded (typical values of $D=d_r=0.025$ were used in most simulations). Almost all the results presented below are for suspensions of pushers for which $\alpha=-1$, $\gamma=1$. A few simulations are also described for suspensions of pullers ($\alpha > 0$), but do not exhibit any instability, in agreement with the predictions of the stability analysis of Sec. III B.

B. Nonlinear dynamics and pattern formation

To study the development of instability and pattern formation in random suspensions, simulations are performed in which the initial condition is a uniform and isotropic suspension perturbed as

$$\Psi(\mathbf{x}, \phi, 0) = \frac{1}{2\pi} \left[1 + \sum_i \epsilon_i \cos(\mathbf{k}_i \cdot \mathbf{x} + \xi_i) P_i(\phi) \right], \quad (59)$$

where ϵ_i is a random coefficient of small magnitude ($|\epsilon_i| \ll 1$), ξ_i is an arbitrary phase, and $P_i(\phi)$ is a low order polynomial in $\cos \phi$ and $\sin \phi$. In the results presented below, the coefficients ϵ_i were chosen randomly in the interval $[-0.01; 0.01]$, and the polynomials P_i were third-order polynomials with random $O(1)$ coefficients. The initial random perturbation used in the simulations is band limited: Typically only the 15 longest modes are included in Eq. (59).

The typical evolution of a suspension of pushers is shown in Fig. 5, where maps of the mean concentration field c , mean director field \mathbf{n} , active particle shear stress Σ_{xy}^p , and disturbance fluid velocity \mathbf{u} are plotted at various times in a square box of linear dimension $L=50$. In particular, this choice of box dimension ensures that the initial perturbation spans both unstable and stable modes, with roughly the first five wavenumbers yielding linearly unstable modes (cf. Sec. III B). At $t=0$, the imposed distribution contains fluctuations at many length scales, and correspondingly, the mean director field only exhibits correlation over very short scales. At short times, the evolution of the distribution is mainly characterized by the decay of these short-scale fluctuations: Both the concentration field and the shear stress field become smoother, but still exhibit weak fluctuations scaling on the box size. The mean director field and the velocity field also change quite drastically and quickly become very smooth and correlated over scales of the order of the box size. At longer times, both the concentration field and the shear stress field begin to develop strong fluctuations at long wavelengths, typically of the order of the box size, as seen in Figs. 5(b)–5(d). The director and velocity fields remain correlated over large scales. These strong fluctuations are not steady in time: While their magnitude stabilizes as a result of diffusion, the position and shape of the fluctuations keep evolving in time, with dense regions constantly merging, breaking up, and reorganizing. In suspensions of pullers, however, none of these dynamics are observed: In fact, we find that all the fluctuations decay leading at long times to a uniform isotropic suspension with zero disturbance velocity. Note that this decay occurs even when the initial perturbation is of large magnitude.

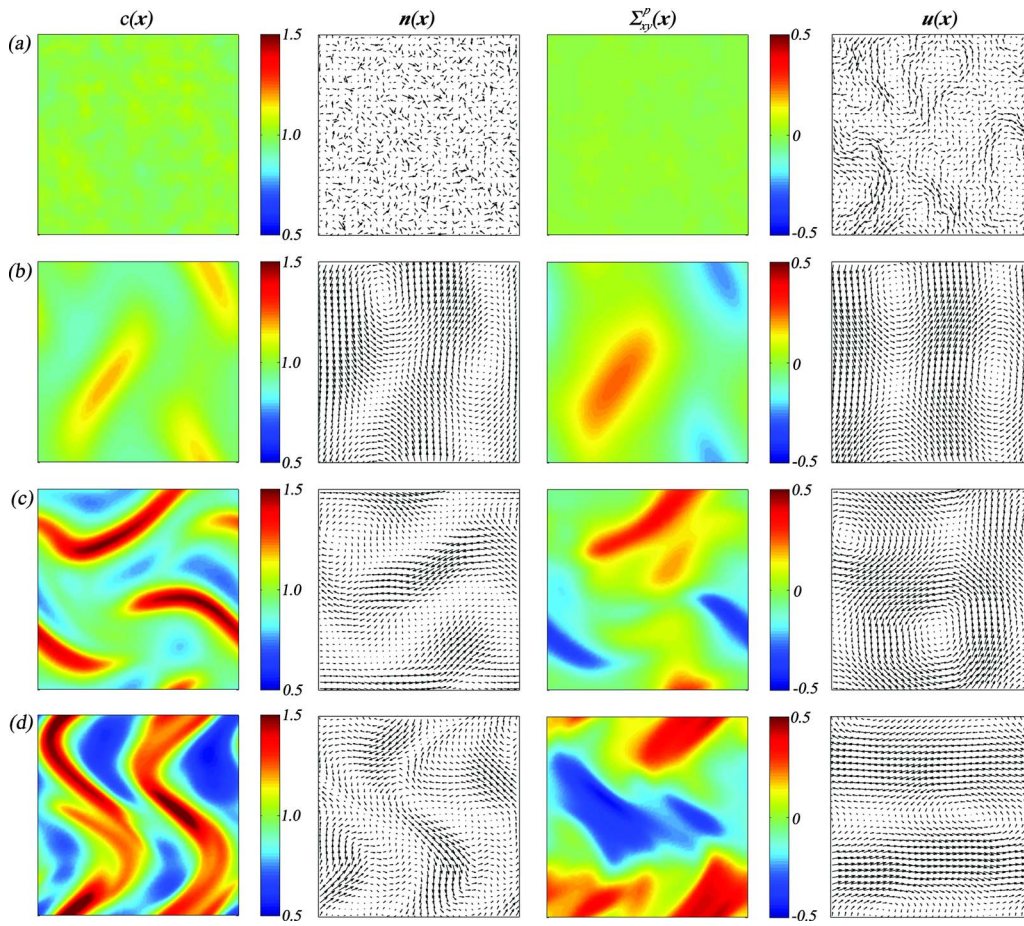


FIG. 5. (Color online) Snapshots of the local concentration c , mean director field \mathbf{n} , active particle shear stress Σ_{xy}^p , and disturbance velocity field \mathbf{u} at various times: (a) $t=0$, (b) $t=50$, (c) $t=100$, and (d) $t=150$. The simulation shown was performed for pushers ($\alpha=-1$, $\gamma=1$) in a square box of linear dimension $L=50$ using 15 random initial modes.

In Fig. 5, the director field \mathbf{n} and the velocity field \mathbf{u} seem to be correlated in some regions. This is confirmed in Fig. 6, which shows the spatially averaged contraction $\langle \mathbf{u} \cdot \mathbf{n} \rangle$ of these two fields, defined as

$$\langle \mathbf{u} \cdot \mathbf{n} \rangle(t) = \int_V c(\mathbf{x}, t) \mathbf{u}(\mathbf{x}, t) \cdot \mathbf{n}(\mathbf{x}, t) d\mathbf{x}. \quad (60)$$

In particular, we find that for pushers, $\langle \mathbf{u} \cdot \mathbf{n} \rangle$, which is initially close to zero, grows to reach a plateau at approximately 0.2. This suggests that pushers tend to align in the local disturbance flow and swim in the direction of the flow. While alignment with the flow was easy to anticipate since the particles align in the local shear according to Jeffery's equation (15), the fact that they on average tend to swim in the direction of the local velocity was *a priori* unexpected and is an interesting result. In particular, this preferred alignment and orientation result in an increase in the effective swimming velocity for pusher particles, a phenomenon already reported in our previous particle simulations.¹⁸ Note that for pullers [Fig. 6(b)], $\langle \mathbf{u} \cdot \mathbf{n} \rangle$ rapidly decays to zero, which is simply a consequence of the quick dissipation of the disturbance flow since no instability takes place in that case.

The various dynamics observed in Fig. 5 are confirmed in Fig. 7, which shows the time evolution of several modes

in the Fourier decomposition of the mean concentration field c , divergence of the concentration-weighted mean director field $\nabla_{\mathbf{x}} \cdot (c\mathbf{n})$, and active particle shear stress Σ_{xy}^p . All three quantities show fairly similar behavior. Initially all Fourier modes are small and of similar magnitudes. As the simulation progresses, high-wavenumber modes [for instance, \mathbf{k}

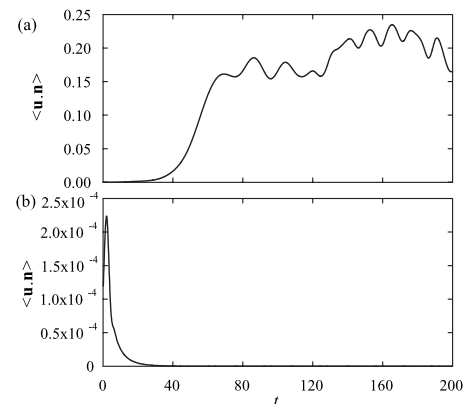


FIG. 6. Spatially averaged contraction of the velocity and director fields $\langle \mathbf{u} \cdot \mathbf{n} \rangle$ [Eq. (60)], in typical simulations of (a) pushers ($\alpha=-1$) and (b) pullers ($\alpha=1$), in a square box of linear dimension $L=50$, using 15 random initial modes.

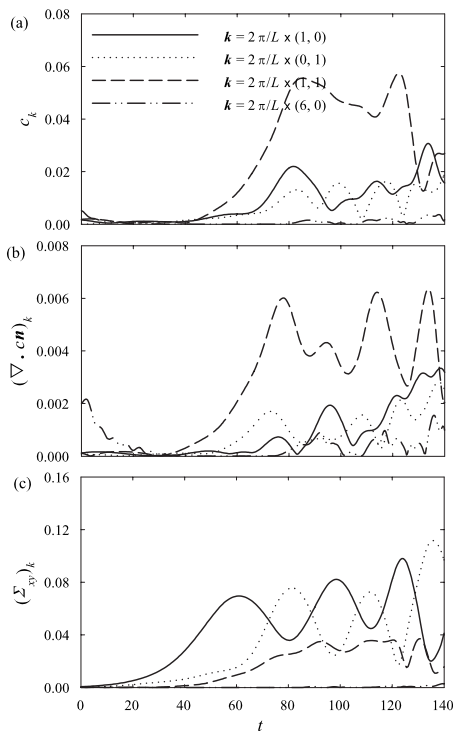


FIG. 7. Time evolution of the magnitude of various Fourier modes of the mean concentration field c , divergence of the concentration-weighted director field $\nabla_{\mathbf{x}} \cdot (c\mathbf{n})$, and active particle shear stress Σ_{xy}^p in the simulation of Fig. 5.

$=2\pi/L \times (6, 0)$ in Fig. 7] are observed to decay, sometimes exhibiting oscillations [in particular, in the case of c and $\nabla_{\mathbf{x}} \cdot (c\mathbf{n})$]. This decay of high-wavenumber modes is followed by the growth of low-wavenumber modes, which very quickly dominate the spectrum. At long times these low-wavenumber modes oscillate, corresponding to the breaking up and merging of the dense regions mentioned above. Another interesting feature observed in Fig. 7 is the time sequence for the growth of these various quantities: In all simulations performed, it is observed that the shear stresses develop first (in agreement with the results of the linear stability analysis), only after which the fluctuations in the divergence of $c\mathbf{n}$ and in the concentration field start to grow.

Many of the dynamics observed in Figs. 5 and 7 can be understood in the light of the stability analysis of Sec. III B. In particular, we found that high-wavenumber stress fluctuations should decay and oscillate, whereas low-wavenumber fluctuations are expected to amplify without any oscillations (Fig. 2). This is consistent with the observations of Fig. 7(c) for the active shear stress. The precise evolution of the concentration field, however, is not predicted by the linear stability. It should also be noted that the fact that the longest wavelength dominates the pattern formation is not simply a consequence of the linear dispersion relation that predicts that the longest modes grow the fastest. In fact, simulations in which only high wavenumbers are present in the initial distribution function (59) also evolve toward the same state as a result of nonlinearities, by which high-wavenumber fluctuations couple nonlinearly to create low-wavenumber modes.

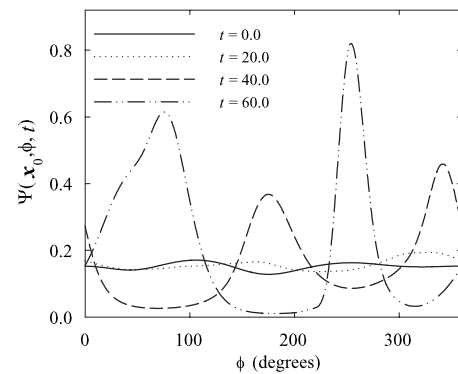


FIG. 8. Orientation distribution at an arbitrary point \mathbf{x}_0 at various times over the course of a simulation. Initially the distribution is nearly uniform (isotropic distribution), but at later times it becomes double peaked, with both peaks separated by approximately 180° (opposite directions).

The evolution of the particle orientations is described more precisely in Fig. 8, showing the orientation distribution at an arbitrary point at various times over the course of a simulation. Initially, the distribution is nearly isotropic, corresponding to the initial condition (59). As the instability develops, it becomes strongly anisotropic and typically presents two peaks separated by approximately 180° , which corresponds to particles pointing in diametrically opposite directions. This suggests a local *nematic* ordering of the particles, which could have been expected from the shear stress instability of Sec. III B, since the active shear stress (6) can be viewed as a nematic order parameter weighted by the local concentration. However, the two peaks typically have different magnitudes, which results in a nonzero net director field \mathbf{n} (i.e., a local *polar* ordering) as observed above in Fig. 5. This observation had already been made in our previous work using direct numerical simulations¹⁸ and is key to understanding the growth of the concentration fluctuations as explained below.

While the stability analysis of Sec. III B was not able to predict the evolution of the concentration field (the linear theory indeed predicts no density fluctuations), the formation of the concentration fluctuations at long times can still be understood by considering Eq. (11). As noted earlier, $-\nabla_{\mathbf{x}} \cdot (c\mathbf{n})$ is the only source term in the evolution equation for the concentration field, which is otherwise simply advected by the disturbance velocity field \mathbf{u} and smoothed by translational diffusion. We should therefore expect any observed density fluctuations to arise due to this term. This can be confirmed by examining maps of the concentration field c and of $\nabla_{\mathbf{x}} \cdot (c\mathbf{n})$ at a given time during a simulation, as shown in Fig. 9. Specifically, Fig. 9 shows these two fields at $t = 50$ during the initial growth of the fluctuations. We indeed find that both fields exhibit similar spatial patterns, and a clear anticorrelation between c and $\nabla_{\mathbf{x}} \cdot (c\mathbf{n})$ can be observed, with convergent regions in the concentration-weighted director field occurring in the more concentrated areas.

The formation of strong density fluctuations in active suspensions had been predicted previously by Simha and Ramaswamy^{27,38} and also observed in our previous direct numerical simulations.¹⁸ The present analysis and simula-

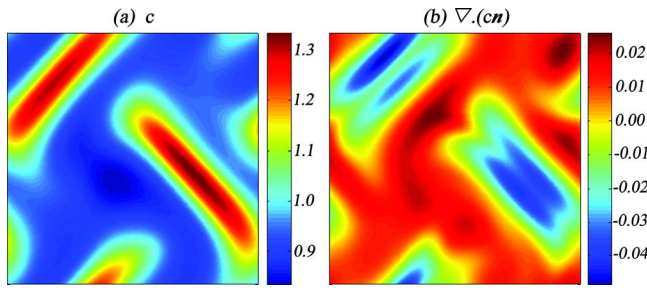


FIG. 9. (Color online) Local concentration field c and divergence of the concentration-weighted director field $\nabla_{\mathbf{x}} \cdot (c\mathbf{n})$ at time $t=50$ in the simulation of Fig. 5. Regions of high concentration are correlated with regions of negative $\nabla_{\mathbf{x}} \cdot (c\mathbf{n})$, suggesting that the concentration fluctuations are driven by evolution of the director field through the swimming of the particles.

tions allow us to explain these density fluctuations as the nonlinear consequence of the shear stress instability. More precisely, the shear stress instability results in the local alignment of the particles over large length scales. While this alignment in principle may only be nematic, the randomness in the suspension always results in local polar ordering, i.e., a nonzero mean director field \mathbf{n} which varies smoothly over large length scales (see Fig. 5, for instance). The resulting concentration-weighted director field $c\mathbf{n}$ is not divergence-free, in general, and since it determines the local direction of the swimming of the particles, it will cause an aggregation of particles in regions where $\nabla_{\mathbf{x}} \cdot (c\mathbf{n}) < 0$ and a depletion in regions where $\nabla_{\mathbf{x}} \cdot (c\mathbf{n}) > 0$, hence the formation of density gradients [cf. Eq. (11)]. The spatial gradients are then stabilized by translational diffusion, while the local alignment is stabilized by rotational diffusion, and the magnitude of the density fluctuations at long times is determined by the balance of these various effects (particle aggregation and diffusion).

At long times, the configuration of the suspension is not steady but constantly fluctuates in time. In particular, we observe that the dense regions are typically in the form of bands as shown in Figs. 5(c) and 5(d). As these bands get denser, they also become unstable and fold onto themselves as is taking place in Fig. 5(d). After folding, they break up and reorganize as new bands in the transverse direction. These dynamics repeat in time in a quasiperiodic fashion, which underlies the slow oscillations in the Fourier modes of the active shear stress in Fig. 7(c). While the precise mechanism leading to the formation and breakup of these bands is not entirely clear, insight can be gained by considering the disturbance flow field, which is shown at two different times in Fig. 10. In Fig. 10(a), shear layers can be observed and surround the dense bands in the concentration field. These layers, however, become unstable and evolve into vortices which cause the breakup of the concentration bands. As the bands reform in the transverse direction, these dynamics repeat in time. An interesting observation is the qualitative similarity between these banded states and the eigenmodes of the linearized problem [compare Fig. 10(a) to Fig. 3], with the caveat that the linear eigenmodes are not associated with concentration fluctuations. Note also that very similar dynamics, with the formation of concentration bands that form

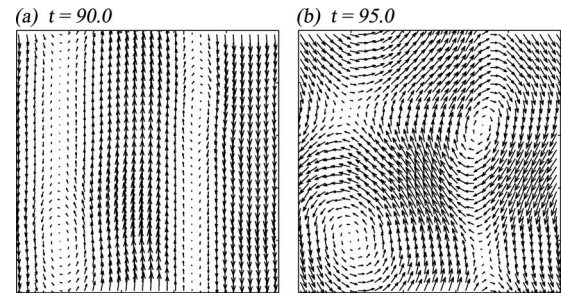


FIG. 10. Disturbance velocity field at two successive times (a) $t=90$ and (b) $t=95$ during a simulation. At $t=90$, shear layers surround the dense concentration bands. These layers become unstable as visible at $t=95$, leading to the formation of vortices that cause the breakup of the bands.

and break up in time, had been observed previously in our direct numerical simulations of periodic suspensions of self-propelled rods.¹⁸ This suggests that these special configurations play a fundamental role in the dynamics of these systems, and we speculate that this phenomenon may also be analogous to the instances of “jetting” previously reported in experiments on bacterial suspensions.^{10,12}

An interesting interpretation of the dynamics can be obtained in terms of the input power generated by the swimming particles in the suspension. Recalling Eqs. (22) and (17), we rewrite Eq. (22) as

$$\int_V 2\mathbf{E}:\mathbf{E}d\mathbf{x} = - \int_V d\mathbf{x} \int_S d\mathbf{p} (\alpha \mathbf{p} \cdot \mathbf{E} \cdot \mathbf{p}) \Psi(\mathbf{x}, \mathbf{p}, t). \quad (61)$$

Again, the left-hand side in Eq. (61) is the rate of viscous dissipation in the fluid, balanced on the right-hand side by the active input power generated by the particles. This allows us to define a local active power density $p(\mathbf{x}, t)$ as

$$p(\mathbf{x}, t) = - \alpha \int_S (\mathbf{p} \cdot \mathbf{E} \cdot \mathbf{p}) \Psi(\mathbf{x}, \mathbf{p}, t) d\mathbf{p}, \quad (62)$$

from which the global input power $P(t)$ is inferred as

$$P(t) = \int_V p(\mathbf{x}, t) d\mathbf{x}. \quad (63)$$

Note that the definition (62) for the power density is consistent with a configuration average of the power generated by self-propelled particles in a micromechanical model for swimming.⁴⁸

An interesting consequence of Eq. (61) is that for pushers ($\alpha < 0$), the input power is largest when the particles are aligned with the axes of extension of the rate-of-strain tensor. This alignment occurs naturally for any particle whose angular dynamics are governed by Jeffery’s equation (15), and we should therefore expect the input power to grow in time in agreement with the existence of an instability. Conversely, in the case of pullers ($\alpha > 0$), we expect any disturbance flow to dissipate rapidly, as otherwise the alignment of the particles with the flow would lead to $p(\mathbf{x}, t) < 0$ and violate the requirement that the rate of viscous dissipation must remain positive in Eq. (61).

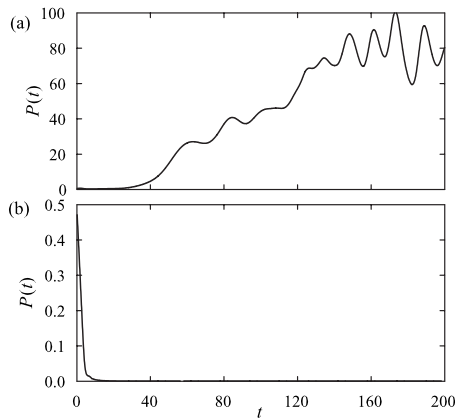


FIG. 11. Global input power $P(t)$ [Eq. (63)] as a function of time in suspensions of (a) pushers ($\alpha=-1$) and (b) pullers ($\alpha=1$).

These observations are indeed confirmed by simulations. Figure 11 shows the evolution of the global input power $P(t)$ during a simulation for both pushers and pullers. As expected, we find that $P(t)$ in suspensions of pullers quickly decays to zero as the disturbance flow dissipates. In suspensions of pushers, $P(t)$ increases with time as the instability takes place, to reach a plateau at long times. It also exhibits oscillations which correspond to the quasiperiodic dynamics described above for the particle configurations. Note also that the power density $p(\mathbf{x}, t)$ is highly nonuniform in space. This is illustrated in Fig. 12(a), which shows $p(\mathbf{x}, t)$ as a function of space at a given time during a simulation of pushers. Figure 12(b) also shows the corresponding plot for the largest eigenvalue $\lambda_{\max}(\mathbf{x})$ of the rate-of-strain tensor \mathbf{E} . As expected from the definition of the power density, we find that $p(\mathbf{x}, t)$ and $\lambda_{\max}(\mathbf{x})$ are strongly correlated, which confirms that the regions where the strongest power is generated are those where fluid stretching is the strongest.

As we showed in Sec. II C, it is the global input power $P(t)$ that drives increases in fluctuations, interpreted in terms of the total system entropy $\mathcal{S}(t)$, which itself grows according to Eq. (23). The system entropy is shown in Fig. 13 for both suspensions of pushers and pullers. As expected, we find that $\mathcal{S}(t)$ grows in the suspension of pullers as the insta-

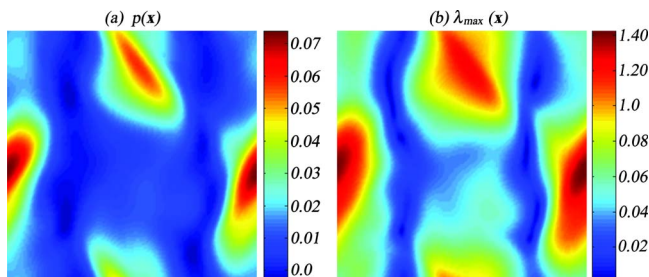


FIG. 12. (Color online) (a) Input power density $p(\mathbf{x})$ and (b) largest eigenvalue $\lambda_{\max}(\mathbf{x})$ of the rate-of-strain tensor \mathbf{E} as a function of position at $t=100$ in a suspension of pushers ($\alpha=-1$). The simulation was performed in a box of linear dimension $L=50$ with 15 random initial modes.

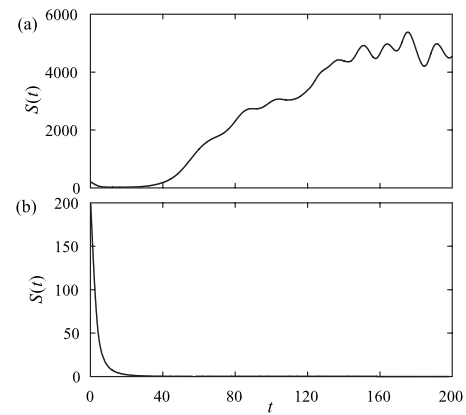


FIG. 13. Total system entropy $\mathcal{S}(t)$ [Eq. (18)] as a function of time in suspensions of (a) pushers ($\alpha=-1$) and (b) pullers ($\alpha=1$).

bility takes place. By $t=150$ the entropy growth has saturated, and the system has presumably entered a state of statistical equilibrium where the active input power is balanced by diffusive processes [cf. Eq. (23)]. In suspensions of pullers, however, $\mathcal{S}(t)$ quickly decays as no instability takes place and becomes almost zero at steady state, which corresponds to a homogeneous isotropic suspension.

All the simulation results presented so far have been obtained in a relatively large simulation box of linear dimension $L=50$ using 15 initial modes, spanning both stable and unstable wavenumbers according to the stability analysis of Sec. III B. Based on this stability analysis, we expect the dynamics to change depending on L , as the simulation size indeed sets the scale for the longest and most unstable modes in the system. Simulations in boxes of other dimensions were therefore also performed. In relatively small boxes, we find that the instability disappears altogether, which corresponds to the case where the smallest wavenumber (or longest wavelength) falls beyond the stability limit found in Fig. 2(b): In that case the dynamics are damped even in the case of pushers, and the disturbance flow introduced by the initial condition simply dissipates.

Qualitatively different dynamics are, however, observed when the system size is chosen to be near the stability limit. In that case, based on the stability analysis of Sec. III B, we expect only the very few longest modes to be unstable and to exhibit oscillations. This is indeed observed in simulations, as depicted in Fig. 14: In a box of dimension $L=17.5$, in which only one mode is linearly unstable, we observe the formation of a low-wavenumber standing wave for the concentration field, which shows an oscillatory behavior in time but never evolves toward the complex dynamics observed in larger boxes (Fig. 5). In particular, the band formation described above is not observed, even at very long times. The quasiperiodic nature of the dynamics in these standing waves is confirmed in Fig. 15, which shows the evolution of two low-wavenumber modes in the Fourier decomposition of the concentration field in the simulation of Fig. 14: The spectrum is dominated by the $\mathbf{k}=2\pi/L \times (1, 1)$ mode, which oscillates periodically and grows in time as a result of the stress instability; at long times its magnitude becomes stabilized by diffusion.

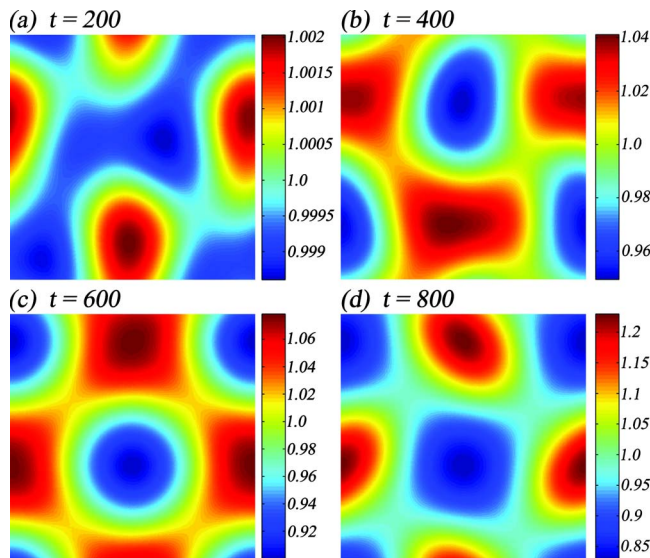


FIG. 14. (Color online) Snapshots of the local concentration field $c(\mathbf{x})$ at various times: (a) $t=200$, (b) $t=400$, (c) $t=600$, and (d) $t=800$, in a square box of linear dimension $L=17.5$, in which we used 15 random modes in the initial condition. With this box dimension, the solution is a two-dimensional standing wave, the amplitude of which grows with time.

C. Fluid mixing

The dynamics described in Sec. IV B, by which concentrated bands grow, become unstable, and break up to reform in the transverse direction, suggest that efficient convective mixing may be taking place. To investigate this further, we consider the evolution of a passive scalar field $s(\mathbf{x}, t)$ which is convected by the disturbance velocity \mathbf{u} as follows:

$$\frac{\partial s}{\partial t} = -\mathbf{u}(\mathbf{x}, t) \cdot \nabla s + d \nabla^2 s, \quad (64)$$

where the diffusive term is added to smooth gradients at short scales and may represent the effects of molecular diffusion. Equation (64) was integrated numerically in time using a semi-implicit fully spectral code, starting from the following initial condition:

$$s_0(\mathbf{x}) = \sin\left(\frac{2\pi y}{L}\right). \quad (65)$$

The evolution of the scalar field during a representative simulation is shown in Fig. 16. At short times, little mixing occurs as the disturbance flow is a nearly uniform and iso-

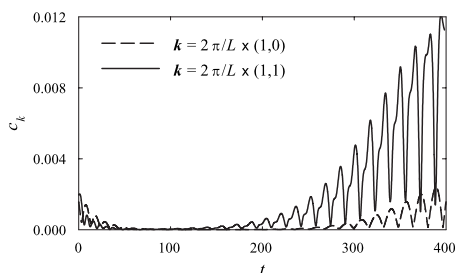


FIG. 15. Time evolution of magnitude of various Fourier modes of the concentration field $c(\mathbf{x})$ in the simulation of Fig. 14.

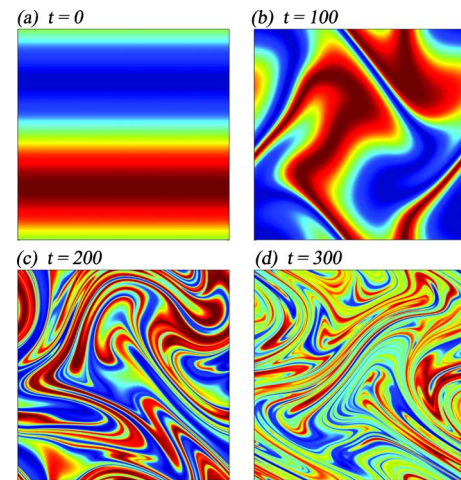


FIG. 16. (Color online) Fluid mixing by an active suspension of pushers ($\alpha=-1$). The figure shows the configuration of a passive scalar field in the suspension at different times: (a) $t=0$, (b) $t=100$, (c) $t=200$, and (d) $t=300$ over the course of a simulation. In this simulation, the scalar diffusivity was set to $d=3 \times 10^{-4}$. The simulation was performed in a box of linear dimension $L=50$ with 15 random initial modes.

tropic suspension is very weak. However, as the instability takes place, the disturbance flow becomes stronger and causes the repeated stretching and folding of fluid elements along the direction of the concentration bands. At $t=200$, patches of uniform color are still visible, albeit much smaller than at earlier times as a few stretch-fold cycles have already taken place. At $t=300$, most of the patches have disappeared and fairly good mixing has already been achieved. Figure 17 also shows the evolution of the maximum value s_{\max} of the scalar field for the same simulation. At short times before the onset of the instability, s_{\max} only decreases very slowly as a result of the scalar diffusivity d . As convective mixing begins to take place, s_{\max} starts decreasing much more rapidly as stronger spatial gradients appear and allow diffusion to smooth s (note that in the case $d \equiv 0$, s_{\max} would be expected to remain 1).

To assess the actual mixing in the simulation of Fig. 16 more quantitatively, we calculate the following multiscale norm for the scalar field s :

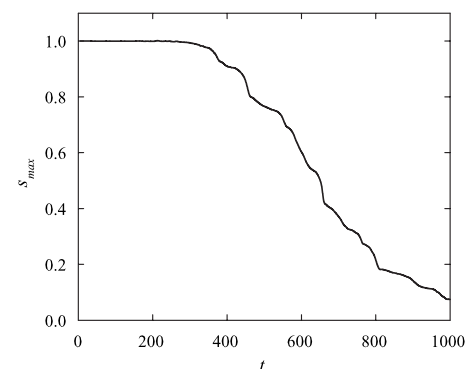


FIG. 17. Evolution of the maximum value s_{\max} of the scalar field $s(\mathbf{x}, t)$ in the simulation of Fig. 16.

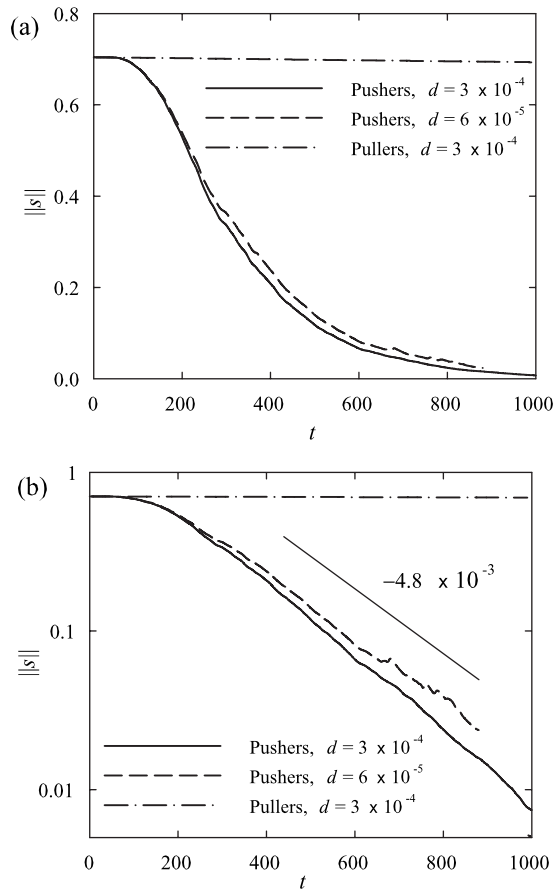


FIG. 18. Time evolution of the multiscale mixing norm $\|s\|$ defined by Eq. (66) for a passive scalar field convected by the disturbance velocity field in an active suspension: (a) linear plot and (b) semilog plot. Results for both suspensions of pushers and pullers are shown. Mixing (as demonstrated by the exponential decay of the norm) is only found to occur in the case of pushers.

$$\|s\| = \left[\sum_{\mathbf{k}} \frac{1}{(1+k^2)^{1/2}} |s_{\mathbf{k}}|^2 \right]^{1/2}, \quad (66)$$

where $s_{\mathbf{k}}$ denotes the Fourier coefficient at wavevector \mathbf{k} in a Fourier expansion of the scalar field. In particular, $\|s\|$ can be shown to be mathematically equivalent to the mixing norm defined by Mathew *et al.*^{49,50} This norm is shown as a function of time in Fig. 18, and we find that in suspensions of pushers it decays with time to become almost zero at long times, an indication of good mixing. More specifically, we find that the decay is exponential, with an exponent of approximately -4.8×10^{-3} in the case $d=6 \times 10^{-4}$. This exponent depends weakly on the chosen value of the scalar diffusivity d and is slightly higher for higher diffusivities as expected. Note, however, that up to $t=400$ the decay of $\|s\|$ is mainly the consequence of convective mixing and not of diffusion, since no significant decrease in s_{\max} has occurred yet. Figure 18 also shows the evolution of $\|s\|$ in a suspension of pullers (for the same simulation parameters), and no significant decay of the norm is observed, suggesting that no mixing occurs: This was expected as no instability takes place in suspensions of pullers and any large-scale flow is damped very rapidly before it can significantly affect the scalar field.

Fluid mixing in active suspensions has been reported in experiments and may present uses for technological applications in which efficient mixing is required but cannot be achieved using inertia.⁹ Our simulations cast light on one origin of mixing on the macroscopic scale, which is related to the constant breakup and merging of concentrated regions as a consequence of the active particle stress instability.

V. CONCLUDING REMARKS

We have used a kinetic model to investigate the dynamics in dilute suspensions of swimming particles. The model, based on a conservation equation for the particle positions and orientations, coupled with fluid flow equations in which the effect of the particles is represented by means of an effective active particle stress tensor, generalizes phenomenological models previously proposed by others.^{27,38} The model was also shown to simplify in situations where particles are polar ordered locally, in which case it reduces to two evolution equations for the local concentration and director fields (both functions of position and time only).

Based on this model, we were able to analyze the linear stability of both aligned and isotropic suspensions. In the aligned case, which had previously been considered by Simha and Ramaswamy,²⁷ we found that the suspensions are always unstable at finite wavelengths as a result of hydrodynamic interactions, in agreement with observations from direct numerical simulations.¹⁸ This result differs from the prediction of Simha and Ramaswamy, who had found that the suspensions were unstable only for some range of wave orientations with a growth rate that did not depend on wavenumber. The reason our model predicts a different result is that it includes full coupling between orientations and local concentration, which had been omitted in the long-wave analysis of Simha and Ramaswamy and results in a different dispersion relation. As the wavenumber goes to zero (infinite wavelength perturbations), the results of Simha and Ramaswamy are recovered by our model.

The case of an isotropic and uniform suspension had not been addressed in detail previously, and a linear stability analysis shows that an instability occurs in these suspensions as well. Rather than pertaining directly to the mean concentration or director fields, the instability concerns the active particle stress exerted by the particles on the fluid. It is found that active shear stresses are unstable at long wavelengths in the case of pushers ($\alpha < 0$). More specifically, low-wavenumber fluctuations are expected to amplify exponentially at short times. Intermediate wavenumbers should amplify as well, albeit at a lower rate, and may exhibit oscillations. Finally, high-wavenumber fluctuations will decay while also exhibiting oscillations. In particular, according to this theory, the longest wavelengths in the system (set by the dimensions of the container) are expected to grow the fastest and therefore dominate the dynamics.

The long-time evolution of the suspensions and, in particular, the pattern formation of the instabilities are not predicted by the linear theory and were addressed using nonlinear simulations of the kinetic equations in two dimensions. The results of the linear stability analysis in the isotropic

case were confirmed, and large-scale shear stress fluctuations are indeed observed to grow. These correspond to a local alignment of the particles (since the particle active stress is directly related to the nematic order parameter in the suspension), which manifests itself by the formation of large-scale correlated regions in the mean director field. Because the mean director field, which determines the swimming direction of the particles relative to the fluid velocity, is not divergence-free, particles aggregate in regions of negative $\nabla_{\mathbf{x}} \cdot (\mathbf{c}\mathbf{n})$, resulting in strong concentration fluctuations over large length scales, in agreement with previous predictions²⁷ and experimental observations.¹² These fluctuations are dynamically unstable and constantly break up and merge in time in a quasiperiodic fashion. An important consequence of these flows is the efficient fluid mixing that results in agreement with previous experiments and simulations:^{9,16} in the present work we characterized mixing by looking at the evolution of a passive scalar and evaluating its level of mixedness using a multiscale mixing norm. In particular, we found that efficient mixing takes place in suspensions of pushers (such as *E. Coli* or *B. Subtilis*) but should not occur in suspensions of pullers (such as *Chlamydomonas*): This prediction has yet to be tested experimentally, as almost all previous studies have used pusher particles.

The present study has focused on bulk suspensions, in which boundary effects and external fields or flows can be neglected. This allowed us to identify intrinsic mechanisms leading to the formation of large-scale inhomogeneities in active suspensions in a general and idealized setting. Other interesting effects are known to occur when such suspensions are placed in confined geometries^{16,18} or in a gravitational field:^{20,12} these situations could also be tackled numerically using our kinetic model, by solving the governing equations with the appropriate boundary conditions and by introducing additional terms capturing the effects of external fields such as gravity on the particle and fluid dynamics. Our current model is also limited to dilute suspensions in which interactions between particles are adequately captured by a mean-field description of the disturbance flow: In more concentrated suspensions, other effects related to near-field interactions may become relevant and would require improvements to our formulation.⁵¹

ACKNOWLEDGMENTS

The authors thank R. Goldstein and C. Hohenegger for useful conversations and gratefully acknowledge the hospitality and support of the Aspen Center for Physics, where part of this work was performed. This work is supported by NSF Grant Nos. DMS-0412203 and DMS-0652775 and DOE Grant No. DE-FG02-88ER25053.

¹T. J. Pedley and J. O. Kessler, "Hydrodynamic phenomena in suspensions of swimming microorganisms," *Annu. Rev. Fluid Mech.* **24**, 313 (1992).

²N. A. Hill and T. J. Pedley, "Bioconvection," *Fluid Dyn. Res.* **37**, 1 (2005).

³W. F. Paxton, K. C. Kistler, C. C. Olmeda, A. Sen, S. K. St. Angelo, Y. Cao, T. E. Mallouk, P. E. Lammert, and V. H. Crespi, "Catalytic nanomotors: Autonomous movement of striped nanorods," *J. Am. Chem. Soc.* **126**, 13424 (2004).

⁴R. Golestanian, T. B. Liverpool, and A. Ajdari, "Propulsion of a molecular machine by asymmetric distribution of reaction products," *Phys. Rev. Lett.* **94**, 220801 (2005).

⁵R. Dreyfus, J. Baudry, M. L. Roper, H. A. Stone, M. Fermigier, and J. Bibette, "Microscopic artificial swimmers," *Nature (London)* **437**, 862 (2005).

⁶T. S. Yu, E. Lauga, and A. E. Hosoi, "Experimental investigations of elastic tail propulsion at low Reynolds number," *Phys. Fluids* **18**, 091701 (2006).

⁷J. R. Howse, R. A. L. Jones, A. J. Ryan, T. Gough, R. Vafabakhsh, and R. Golestanian, "Self-motile colloidal particles: from directed propulsion to random walk," *Phys. Rev. Lett.* **99**, 048102 (2007).

⁸X.-L. Wu and A. Libchaber, "Particle diffusion in a quasi-two-dimensional bacterial bath," *Phys. Rev. Lett.* **84**, 3017 (2000).

⁹M. J. Kim and K. S. Breuer, "Enhanced diffusion due to motile bacteria," *Phys. Fluids* **16**, L78 (2004).

¹⁰N. H. Mendelson, A. Bourque, K. Wilkening, K. R. Anderson, and J. C. Watkins, "Organized cell swimming motions in *Bacillus subtilis* colonies: Patterns of short-lived whirls and jets," *J. Bacteriol.* **181**, 600 (1999).

¹¹G. V. Soni, B. M. Jaffar Ali, Y. Hatwalne, and G. V. Shivashankar, "Single particle tracking of correlated bacterial dynamics," *Biophys. J.* **84**, 2634 (2003).

¹²C. Dombrowski, L. Cisneros, S. Chatkaew, R. E. Goldstein, and J. O. Kessler, "Self-concentration and large-scale coherence in bacterial dynamics," *Phys. Rev. Lett.* **93**, 098103 (2004).

¹³I. Tuval, L. Cisneros, C. Dombrowski, C. W. Wolgemuth, J. O. Kessler, and R. E. Goldstein, "Bacterial swimming and oxygen transport near contact lines," *Proc. Natl. Acad. Sci. U.S.A.* **102**, 2277 (2005).

¹⁴L. H. Cisneros, R. Cortez, C. Dombrowski, R. E. Goldstein, and J. O. Kessler, "Fluid dynamics of self-propelled microorganisms, from individuals to concentrated populations," *Exp. Fluids* **43**, 737 (2007).

¹⁵A. Sokolov, I. S. Aranson, J. O. Kessler, and R. E. Goldstein, "Concentration dependence of the collective dynamics of swimming bacteria," *Phys. Rev. Lett.* **98**, 158102 (2007).

¹⁶J. P. Hernández-Ortiz, C. G. Stoltz, and M. D. Graham, "Transport and collective dynamics in suspensions of confined self-propelled particles," *Phys. Rev. Lett.* **95**, 204501 (2005).

¹⁷P. T. Underhill, J. P. Hernández-Ortiz, and M. D. Graham, "Divergent diffusivity and long-range correlations in suspensions of swimming particles," *Phys. Rev. Lett.* **100**, 248101 (2008).

¹⁸D. Saintillan and M. J. Shelley, "Orientational order and instabilities in suspensions of self-locomoting rods," *Phys. Rev. Lett.* **99**, 058102 (2007).

¹⁹S. Childress, M. Levandowsky, and E. A. Spiegel, "Pattern formation in a suspension of swimming microorganisms: Equations and stability theory," *J. Fluid Mech.* **69**, 591 (1975).

²⁰M. M. Hopkins and L. J. Fauci, "A computation model of the collective fluid dynamics of motile micro-organisms," *J. Fluid Mech.* **455**, 149 (2002).

²¹N. G. Cogan and C. W. Wolgemuth, "Pattern formation by bacteria-driven flow," *Biophys. J.* **88**, 2525 (2005).

²²N. Sambelashvili, A. W. C. Lau, and D. Cai, "Dynamics of bacterial flow: Emergence of spatiotemporal coherent structures," *Phys. Lett. A* **360**, 507 (2007).

²³C. Brennen and H. Winet, "Fluid mechanics of propulsion by cilia and flagella," *Annu. Rev. Fluid Mech.* **9**, 339 (1977).

²⁴A. Ajdari and H. A. Stone, "A note on swimming using internally generated traveling waves," *Phys. Fluids* **11**, 1275 (1999).

²⁵E. Gouin, M. D. Welch, and P. Cossart, "Actin-based motility of intracellular pathogens," *Curr. Opin. Microbiol.* **8**, 35 (2005).

²⁶A. M. Leshansky, "Actin-based propulsion of a microswimmer," *Phys. Rev. E* **74**, 012901 (2006).

²⁷R. A. Simha and S. Ramaswamy, "Hydrodynamic fluctuations and instabilities in ordered suspensions of self-propelled particles," *Phys. Rev. Lett.* **89**, 058101 (2002).

²⁸D. Saintillan and M. J. Shelley, "Instabilities and pattern formation in active particle suspensions: Kinetic theory and continuum simulations," *Phys. Rev. Lett.* **100**, 178103 (2008).

²⁹T. Ishikawa, M. P. Simmonds, and T. J. Pedley, "Hydrodynamic interaction of two swimming model micro-organisms," *J. Fluid Mech.* **568**, 119 (2006).

- ³⁰T. Ishikawa and T. J. Pedley, "Diffusion of swimming model micro-organisms in a semi-dilute suspension," *J. Fluid Mech.* **588**, 437 (2007).
- ³¹T. Ishikawa and T. J. Pedley, "The rheology of a semi-dilute suspension of swimming model micro-organisms," *J. Fluid Mech.* **588**, 399 (2007).
- ³²T. Ishikawa, T. J. Pedley, and T. Yamaguchi, "Orientational relaxation time of bottom-heavy squirmers in a semi-dilute suspension," *J. Theor. Biol.* **249**, 296 (2007).
- ³³T. Ishikawa and T. J. Pedley, "Coherent structures in monolayers of swimming particles," *Phys. Rev. Lett.* **100**, 088103 (2008).
- ³⁴G. K. Batchelor, "Slender-body theory for particles of arbitrary cross-section in Stokes flow," *J. Fluid Mech.* **44**, 419 (1970).
- ³⁵A. Czirók, A.-L. Barabási, and T. Vicsek, "Collective motion of self-propelled particles: Kinetic phase transition in one dimension," *Phys. Rev. Lett.* **82**, 209 (1999).
- ³⁶J. Toner, Y. Tu, and S. Ramaswamy, "Hydrodynamics and phases of flocks," *Ann. Phys.* **318**, 170 (2005).
- ³⁷R. A. Simha and S. Ramaswamy, "Statistical hydrodynamics of ordered suspensions of self-propelled particles: waves, giant number fluctuations and instabilities," *Physica A* **306**, 262 (2002).
- ³⁸S. Ramaswamy and R. A. Simha, "The mechanics of active matter: Broken-symmetry hydrodynamics of motile particles and granular layers," *Solid State Commun.* **139**, 617 (2006).
- ³⁹D. L. Koch and E. S. G. Shaqfeh, "The instability of a dispersion of sedimenting spheroids," *J. Fluid Mech.* **209**, 521 (1989).
- ⁴⁰D. Saintillan, E. S. G. Shaqfeh, and E. Darve, "The effect of stratification on the wave number selection in the instability of sedimenting spheroids," *Phys. Fluids* **18**, 121503 (2006).
- ⁴¹M. Doi and S. F. Edwards, *The Theory of Polymer Dynamics* (Oxford University Press, Oxford, 1986).
- ⁴²G. B. Jeffery, "The motion of ellipsoidal particles immersed in a viscous fluid," *Proc. R. Soc. London, Ser. A* **102**, 161 (1922).
- ⁴³F. P. Bretherton, "The motion of rigid particles in a shear flow at low Reynolds number," *J. Fluid Mech.* **14**, 284 (1962).
- ⁴⁴G. K. Batchelor, "The stress generated in a non-dilute suspension of elongated particles by pure straining motion," *J. Fluid Mech.* **46**, 813 (1971).
- ⁴⁵F. Otto and A. Tzavaras, "Continuity of velocity gradients in suspensions of rod-like molecules," *Commun. Math. Phys.* **277**, 729 (2008).
- ⁴⁶T. J. Pedley, personal communication (Nov. 18, 2007).
- ⁴⁷C. Hohenegger and M. J. Shelley, personal communication (May 22, 2008).
- ⁴⁸For a self-propelled rodlike particle exerting a force distribution $\mathbf{f}(s\mathbf{p})$ on the fluid (where s is a linear coordinate along the particle axis), a natural definition for the local power density is $p(\mathbf{x}) = \int d\mathbf{p} \Psi(\mathbf{x}, \mathbf{p}) \int ds \mathbf{f}(s\mathbf{p}) \cdot \mathbf{u}(\mathbf{x} + s\mathbf{p})$. Linearizing the force distribution and the fluid velocity along the axis of the particle as $\mathbf{f}(s\mathbf{p}) \propto s\mathbf{p}$ and $\mathbf{u}(\mathbf{x} + s\mathbf{p}) \approx \mathbf{u}(\mathbf{x}) + s\mathbf{p} \cdot \nabla \mathbf{u}(\mathbf{x})$, we obtain for the power density, $p(\mathbf{x}) \propto \int d\mathbf{p} \Psi(\mathbf{x}, \mathbf{p}) (\mathbf{p} \cdot \mathbf{E} \cdot \mathbf{p})$, where the proportionality constant can be shown to be precisely $-\alpha$, in agreement with Eq. (62); cf. Ref. 18.
- ⁴⁹G. Mathew, I. Mezić, and L. Petzold, "A multiscale measure for mixing," *Physica D* **211**, 23 (2005).
- ⁵⁰G. Mathew, I. Mezić, S. Grivopoulos, U. Vaidya, and L. Petzold, "Optimal control of mixing in Stokes fluid flows," *J. Fluid Mech.* **580**, 261 (2007).
- ⁵¹I. S. Aranson, A. Sokolov, J. O. Kessler, and R. E. Goldstein, "Model for dynamical coherence in thin films of self-propelled microorganisms," *Phys. Rev. E* **75**, 040901 (2007).